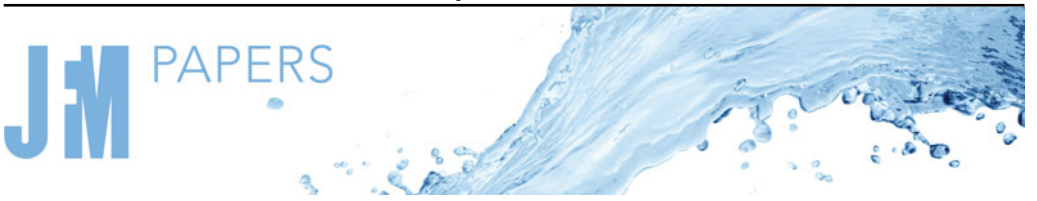
J. Fluid Mech. (2026), *vol.* 1038, A9, doi:10.1017/jfm.2026.11746



Deformation and motion of a thin sessile drop in shear flow

Xi-Hu Wu[1], **Hang Ding**[1] **and Peng Gao**[1]

[1]State Key Laboratory of High Temperature Gas Dynamics, School of Engineering Science, University of Science and Technology of China, Hefei, Anhui 230026, PR China

Corresponding author: Peng Gao, gaopeng@ustc.edu.cn

(Received 25 December 2025 UTC; revised 18 May 2026 UTC; accepted 28 May 2026 UTC)

Drop deformation and motion driven by shear flows are widespread phenomena in nature and underpin a variety of technological applications. We investigate the deformation, motion and contact-line dynamics of two-dimensional drops in steady shear flows within the framework of lubrication theory. For pinned drops with 180° hysteresis, we identify a critical shear rate, beyond which the upstream side becomes unstable and a thinning film develops. At late stage, the thinning film connects to the bulk drop through a self-similar capillary transition structure. For moving drops with 0° hysteresis, the dynamical behaviours can be classified into three regions: in the low-shear region, the steady-state drop velocity increases linearly with the shear number S; in the intermediate-shear region, the drop velocity exhibits a non-monotonic dependence on S; in the high-shear region, the steady-state drop profile can be clearly divided into the entrained film, dimple and capillary ridge. Moreover, during the drop evolution under high shear, a Landau–Levich–Derjaguin-like (LLD-like) film emerges and exhibits a scaling law that differs from the classical LLD law. These results provide a unified theoretical and numerical framework for understanding shear-driven drop dynamics and may offer insights into analogous three-dimensional systems.

Key words: drops, contact lines, thin films

1. Introduction

The deformation and motion of drops are ubiquitous in nature and can be driven by a variety of physical mechanisms. Common driving effects include gravity, shear flows, centrifugal forces, Marangoni effects, electrowetting and evaporation-driven capillary flows (Spelt 2006; Ahmadlouydarab & Feng 2014; Benilov & Benilov 2015; Andreotti & Snoeijer 2020; Pan *et al.* 2022). The associated drop dynamics also plays a critical role in various industrial processes, such as inkjet printing, surface coating, microfluidic device

© The Author(s), 2026. Published by Cambridge University Press.

https://doi.org/10.1017/jfm.2026.11746 Published online by Cambridge University Press

fabrication and photoresist patterning (Castrejón-Pita *et al.* 2016; Lohse 2022; Sprittles 2024).

Studies of sessile drop dynamics commonly involve two representative types of contact-line behaviours: pinned and moving contact lines. A key factor controlling the transition between the two behaviours is contact-angle hysteresis, defined as $\Delta\theta = \theta_A - \theta_R$, where θ_A and θ_R are the advancing and receding contact angles, respectively. Contact-angle hysteresis arises from energy barriers associated with surface roughness or chemical heterogeneity, which immobilise the contact line at microscale defects (Varagnolo *et al.* 2013; Savva, Groves & Kalliadasis 2019). Under an applied driving force, a sessile drop initially deforms, but if the contact angle θ remains within $[\theta_R, \theta_A]$, the contact line stays pinned; contact-line motion occurs only when θ exceeds this range. A moving contact line poses theoretical difficulties, as the classical no-slip boundary condition leads to a singularity in both viscous stress and pressure at the contact lines (Huh & Scriven 1971; Dussan & Davis 1974). Slip models have been widely adopted to regularise this singularity, in which multiple length scales – from the capillary length (millimetre scale) down to molecular scales (nanometre scale), spanning approximately six orders of magnitude – are inherently involved (Bonn *et al.* 2009; Snoeijer & Andreotti 2013; Sui, Ding & Spelt 2014; Sibley, Nold & Kalliadasis 2015). For drops with pinned contact lines, variations in the microscopic contact angle can significantly influence the macroscopic behaviour of the drop (Bernis, Hulshof & King 2000; Eggers & Fontelos 2025). Accurate modelling of pinning therefore requires a careful description of the dynamic evolution of the contact angle at the microscale.

Drop depinning, deformation and motion in shear flow have been studied to understand the fundamental physics of interface-driven transport and adhesion. Early theoretical efforts, using lubrication theory in the low-Reynolds-number regime, established that the critical flow velocity gradient depends on the drop's surface tension, volume, contact-angle hysteresis and the viscosity of the shearing fluid, but is independent of the drop's own viscosity (Dussan 1987). By assuming a completely pinned contact line, Li & Pozrikidis (1996) identified a critical capillary number beyond which continuous deformation occurs until the apparent contact angle exceeds the hysteresis limits. Dimitrakopoulos & Higdon (1997, 1998) and Dimitrakopoulos (2007*a*,*b*) subsequently incorporated gravity, large contact angles, viscosity ratios and inertia, revealing that the critical flow velocity gradient depends strongly on the viscosity ratio, with viscous and inviscid drops exhibiting qualitatively distinct behaviours. The influence of inertia at higher Reynolds numbers was further addressed by considering pressure drag and aerodynamic forces in sessile drops (Durbin 1988), and through numerical simulations of two- and three-dimensional drops in moderate-Reynolds-number shear flows (Spelt 2006; Ding & Spelt 2008; Ding, Gilani & Spelt 2010). These studies showed that, while inertia markedly alters the critical flow velocity gradient, the steady drop shape remains similar to that in creeping flow, and that a narrow range of critical capillary numbers can trigger entrainment, breakup or complete detachment (Ding & Spelt 2008; Ding *et al.* 2010). Moreover, in high-Reynolds-number shear flows, the depinning threshold also depends on drop volume, the direction of gravity relative to the flow and flow separation around the drop (Hooshanginejad & Lee 2022).

While the aforementioned studies focus primarily on Newtonian drops on homogeneous substrates, complex factors such as viscoelasticity, surfactants and substrate heterogeneity also significantly alter the drop dynamics in shear flows. Gupta & Sbragaglia (2014) and Wang *et al.* (2023) studied viscoelastic effects on drop deformation, motion and breakup, showing that polymer extensibility and confinement affect interface stability and breakup thresholds under shear. Surfactants could enhance drop deformation and motion through Marangoni effects and reduce the critical capillary numbers for breakup and detachment

https://doi.org/10.1017/jfm.2026.11746 Published online by Cambridge University Press

(Yon & Pozrikidis 1999; Liu *et al.* 2020; Shang *et al.* 2022). On rough substrates, the critical pressure gradient for depinning is governed by the viscosity ratio, wettability and drop volume, with the maximum slope of surface defects playing a decisive role in depinning and residual drop formation (Mhatre & Kumar 2024).

Alongside these theoretical and numerical studies, experiments have confirmed and extended the understanding of drop deformation, depinning and motion. Channel-flow and wind-tunnel measurements demonstrate that the depinning threshold is primarily controlled by surface wettability and drop size, while internal viscosity plays a secondary role (Lu *et al.* 2019; Wang *et al.* 2022). Beyond the onset of motion, Fan, Wilson & Kapur (2011) identified three motion modes: footprint-preserving translation, tail formation and trailing with satellite drop shedding, which were also observed by Seevaratnam *et al.* (2010) and Madani & Amirfazli (2014), who investigated the shedding of oil drops under varying flow rates and viscosity ratios. Recent experiments have further linked the internal dynamics and substrate architecture to drop removal, showing that oscillatory motion inside the drop generates inertial forces that aid contact-line depinning (Mortazavi & Jung 2023), and that textured surfaces enhance drop removal by strongly influencing the shear-induced steady velocity through wettability, drop size and air speed (Xu *et al.* 2024).

While the above studies have significantly advanced our understanding of drop motion, adhesion and depinning under shear through both simulations and experiments, a comprehensive understanding of the coupled evolution of drop shape and contact line remains limited. In particular, whether a drop with a small contact angle will eventually evolve toward detachment when the shear exceeds the critical value remains to be investigated.

This work aims to perform a systematic analytical and numerical investigation of the deformation and motion of two-dimensional thin sessile drops in shear flow, within the framework of lubrication theory. Although two-dimensional drops are generally unstable in physical systems due to transverse perturbations, their fundamental dynamical behaviour shares many features with three-dimensional drops (Huppert 1982; Thiele & Knobloch 2003). For example, experiments confirmed that a thin trailing film forms at the rear of the drop at higher shear rates (Fan *et al.* 2011; Xu *et al.* 2024), and once a critical shear threshold is exceeded, the drop velocity increases only weakly with further increases in shear (Fan *et al.* 2011). From a modelling perspective, the two-dimensional drop thus serves as a useful theoretical platform that can inform and support subsequent studies of three-dimensional systems (Dussan 1987; Benilov & Benilov 2015). The lubrication approximation, which greatly simplifies the governing equations via the thin-drop and small-contact-angle assumption, has been widely applied to modelling thin-film flows such as spin coating, dip coating and gravity-driven drop motion (Oron, Davis & Bankoff 1997; Benilov & Benilov 2015; Kang, Nadim & Chugunova 2016; Qin & Gao 2018; Mhatre & Kumar 2024). The resulting predictions are generally considered valid for moderate contact angles. The flow within the drop is assumed to occur at low Reynolds number, and the flow near the substrate can be approximated as a linear shear profile. These assumptions (thin two-dimensional drop, small contact angles, creeping flow and linear shear flow) reduce the problem to a reduced set of governing parameters while still capturing the essential drop dynamics in shear flow.

We consider two canonical cases: drops with pinned contact lines, and drops with moving contact lines. Employing a Navier-slip model and defining a dimensionless shear number as the main control parameter, we combine asymptotic analysis and numerical methods to explore how drop velocity, shape and interface profile depend on shear. The results reveal different structural regimes and scaling laws that describe how drops behave in shear flows.

https://doi.org/10.1017/jfm.2026.11746 Published online by Cambridge University Press

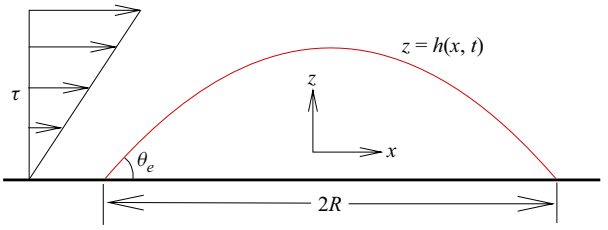


Figure 1. A two-dimensional thin drop, initially at rest with a parabolic profile, is subjected to a steady shear stress.

The paper is organised as follows. The problem statement and governing equation are introduced in § 2. In § 3, we investigate the drops with pinned contact lines at both ends, dividing the analysis into three regimes: low shear, critical shear and high shear. In § 4, we examine the drops with moving contact lines, also considering three regimes: low shear, intermediate shear and high shear. Conclusions are drawn in § 5.

2. Formulation

We consider a two-dimensional Newtonian drop resting on a substrate, initially maintaining an equilibrium parabolic shape, as shown in figure 1. The liquid is of constant viscosity μ, density ρ and surface tension σ. The surface of the drop intersects the substrate with a contact angle θ_e, which is assumed small such that the lubrication approximation can be used. It should be noted that for a drop with both contact lines pinned, θ_e represents the initial equilibrium contact angle, while θ_e is also the microscopic contact angle (assumed equal to the static contact angle) for the moving contact-line case. The length of the drop is $2R$, corresponding to a dimensional volume $V_{dim} = 2R^2\theta_e/3$. The drop is subjected to a shear flow of an immiscible fluid over its surface. The drop is thin and small relative to the characteristic length scale of the external flow, so that the flow can be locally approximated as a linear shear. For small drops at low Reynolds numbers, the inertia of the external flow is negligible. The surface position is $z = h(x, t)$, where x is the horizontal coordinate and t is time.

Under the lubrication approximation, the shear stress τ exerted on the drop surface is assumed to be uniformly distributed, with no distinction between the upstream and downstream sides (Oron *et al.* 1997). At leading order, the motion of the fluid inside the drop is effectively decoupled from the surrounding flow (Dussan 1987), and the stress balance at the surface can be written as

$$p_0 - p = \sigma \frac{\partial^2 h}{\partial x^2}, \tag{2.1}$$

$$\mu \frac{\partial u}{\partial z} = \tau, \tag{2.2}$$

where u is the horizontal component of the velocity and p is the pressure of the liquid; p_0 is the atmospheric pressure, which is assumed constant.

We consider two contact-line behaviours, which correspond to two idealised limits of contact-angle hysteresis. The pinned case represents very strong pinning (effectively a 180° hysteresis), with the contact line fixed under any applied shear force, while the moving case corresponds to negligible hysteresis (effectively a 0° hysteresis), with the contact line responding immediately to shear on a smooth, chemically homogeneous surface.

https://doi.org/10.1017/jfm.2026.11746 Published online by Cambridge University Press

2.1. *Drops with moving contact lines*

Both the precursor-film and Navier-slip models are commonly used to regularise the viscous stress singularity at moving contact lines (Huh & Scriven 1971; Sibley *et al.* 2015). The precursor-film model is particularly suitable for problems involving free-surface topological changes such as breakup or rupture (Mhatre & Kumar 2024), whereas the Navier-slip model is more straightforward and conceptually simpler. For the present two-dimensional drop deformation and motion problem with moving contact lines, we therefore adopt the Navier-slip model (see, Hocking 1983; Eggers 2005; Snoeijer & Andreotti 2013; Qin, Lu & Gao 2024). The slip length is denoted by λ, which is typically a few nanometres. Then, following the procedure outlined by Oron *et al.* (1997), we derive the pressure and velocity distributions within the drop as follows:

$$p = \rho g(h - z) - \sigma \frac{\partial^2 h}{\partial x^2} + p_0, \tag{2.3a}$$

$$u = \frac{1}{2\mu}\frac{\partial p}{\partial x}\left(z^2 - 2hz - 2\lambda h\right) + \frac{\tau}{\mu}(z + \lambda), \tag{2.3b}$$

where g is the gravitational acceleration.

Accordingly, the lubrication equation governing the deformation and motion of thin drops reads

$$\frac{\partial h}{\partial t} + \frac{1}{3\mu}\frac{\partial}{\partial x}\left[h^2(h + 3\lambda)\left(\sigma\frac{\partial^3 h}{\partial x^3} + \rho g\frac{\partial h}{\partial x}\right)\right] + \frac{\tau}{2\mu}\frac{\partial}{\partial x}\left[h(h + 2\lambda)\right] = 0. \tag{2.4}$$

Through the scaled variables

$$x = RX, \quad z = R\theta_e Z, \quad h = R\theta_e H, \quad \lambda = R\theta_e \Lambda, \quad t = \frac{3\mu R}{\sigma\theta_e^3}T, \tag{2.5}$$

we non-dimensionalise the governing equation (2.4) to

$$\frac{\partial H}{\partial T} + \frac{\partial}{\partial X}\left[H^2(H + 3\Lambda)\left(\frac{\partial^3 H}{\partial X^3} + Bo\frac{\partial H}{\partial X}\right)\right] + S\frac{\partial}{\partial X}\left[H(H + 2\Lambda)\right] = 0, \tag{2.6}$$

where

$$S = \frac{3\tau R}{2\sigma\theta_e^2} \tag{2.7}$$

is the dimensionless parameter characterising the ratio of shear stress to the surface tension, and the Bond number $Bo = \rho g R^2/\sigma$ characterises the relative importance of gravity to surface tension. We focus on small drops such that the gravitational effect is negligible, i.e. $Bo = 0$.

After non-dimensionalisation, the initial parabolic drop profile reads

$$H_{init} = X - \frac{X^2}{2}, \tag{2.8}$$

indicating that the contact lines are initially located at $X = 0$ and 2.

We assume that the advancing contact angle equals its receding counterpart, i.e. the contact-angle hysteresis is neglected. The fourth-order equation (2.6) is supplemented by the following conditions:

https://doi.org/10.1017/jfm.2026.11746 Published online by Cambridge University Press

$$H=0,\quad \frac{\partial H}{\partial X}=1\quad \text{at}\quad X=L_{rec}(T), \tag{2.9}$$

$$H=0,\quad \frac{\partial H}{\partial X}=-1\quad \text{at}\quad X=L_{adv}(T), \tag{2.10}$$

where $L_{rec}(T)$ and $L_{adv}(T)$ denote the positions of the receding and advancing contact lines, respectively. As the contact lines are moving, additional boundary conditions are required

$$c_{rec}=3\Lambda \lim_{x\to L_{rec}^{+}} H\frac{\partial^3 H}{\partial X^3}+2\Lambda S,\quad c_{adv}=3\Lambda \lim_{x\to L_{adv}^{-}} H\frac{\partial^3 H}{\partial X^3}+2\Lambda S, \tag{2.11}$$

where $c_{adv/rec}\equiv \mathrm{d}L_{adv/rec}/\mathrm{d}t$ represents the advancing/receding contact-line velocity. These conditions guarantee that the contact lines are material lines and can be obtained by calculating the limit of the depth-averaged velocity towards the contact lines.

The governing equation (2.6) together with the initial and boundary conditions (2.8)–(2.11) is solved numerically, with details provided in Appendix A.

2.2. *Drops with pinned contact lines*

Due to chemical heterogeneity, surface roughness or deliberate experimental constraints, a drop may become pinned (see, Savva *et al.* 2019; Lohse 2022; Mhatre & Kumar 2024). In this case, the viscous stress (associated with HH_{XXX}) is not singular in the absence of slip, as inferred from the local asymptotic expansion of the film thickness in Appendix B. Therefore, the slip models are not implemented. Accordingly, the non-dimensional governing equation (2.6) becomes

$$\frac{\partial H}{\partial T}+\frac{\partial}{\partial X}\left(H^3\frac{\partial^3 H}{\partial X^3}\right)+S\frac{\partial}{\partial X}\left(H^2\right)=0. \tag{2.12}$$

The initial drop profile is the same as (2.8). At the contact line, we expect the flux to vanish (Bernis *et al.* 2000; Eggers & Fontelos 2025), yielding the following boundary conditions:

$$H(0,T)=H(2,T)=0,\quad \left(H^3\frac{\partial^3 H}{\partial X^3}+SH^2\right)\Big|_{X=0,2}=0. \tag{2.13}$$

The governing equation (2.12) together with boundary conditions (2.13) is solved numerically, with details provided in Appendix B.

3. Pinned contact-line case: drop deformation

In this case, deformation of the drops is governed only by the shear number S. Numerical results reveal the existence of a critical shear number

$$S_{cr}=0.588. \tag{3.1}$$

When $S\le S_{cr}$, the drop evolves into a steady state; for $S>S_{cr}$, the drop never reaches a steady state, leaving a thinning film on the upstream side.

3.1. *Low shear: $S\le S_{cr}$*

Using the numerical algorithm described in Appendix B.1, we find that, under low shear, a drop evolves from its initial parabolic shape to a steady state. Focusing on the steady state of the drops with the profile $H(X)$, the governing equation (2.12) can be integrated once

https://doi.org/10.1017/jfm.2026.11746 Published online by Cambridge University Press

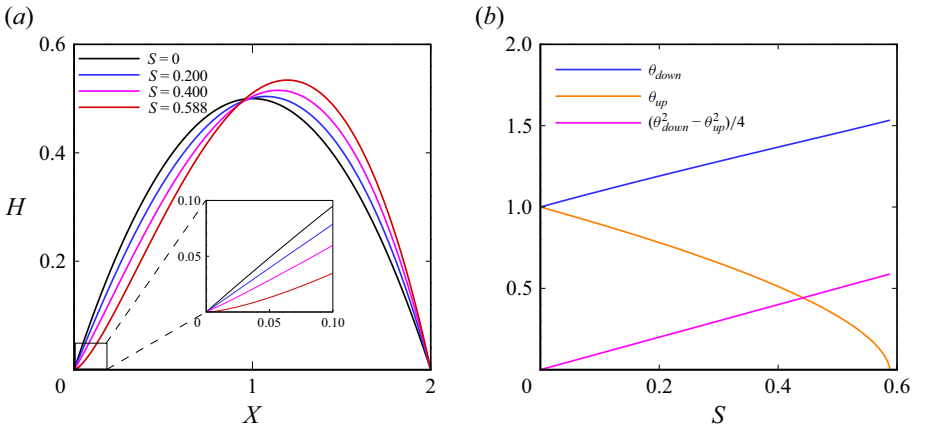


Figure 2. Steady-state pinned drops under low shear obtained from numerical solutions: (*a*) drop profiles; (*b*) variation of the upstream-side microscopic contact angle θ_{up} and downstream-side microscopic contact angle θ_{down} with respect to the shear number S.

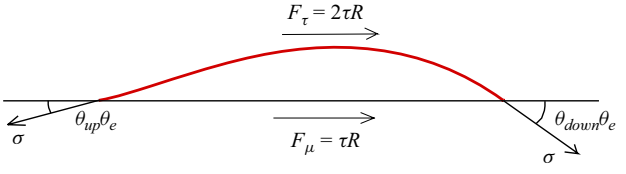


Figure 3. Force balance analysis of a steady drop with pinned contact lines under low shear.

to give

$$HH''' + S = 0, \tag{3.2}$$

where the conditions of vanishing flux have been used. The steady solution can be determined by the conditions of vanishing thickness at the contact lines and mass conservation

$$H(0) = H(2) = 0, \quad \int_0^2 H \, \mathrm{d}X = \frac{2}{3}. \tag{3.3}$$

The steady-state problem (3.2) and (3.3) is solved using the numerical algorithm described in Appendix B.2. The solutions are computed for a sequence of shear numbers S with a uniform increment $\Delta S = 0.001$, from which the steady drop profiles and the corresponding microscopic contact angles are obtained. As shown in figure 2, the steady-state drop profiles lean to the downstream side with increasing shear rate. We denote the upstream-side and downstream-side microscopic contact angles as θ_{up} and θ_{down}, respectively; θ_{up} decreases with increasing shear number S and vanishes at $S = S_{cr}$ and θ_{down} increases with S, reaching a maximum value of 1.534 at $S = S_{cr}$.

To obtain the quantitative relationship among θ_{up}, θ_{down} and S, we perform a force analysis of a steady-state drop, as sketched in figure 3. Considering only the horizontal force balance, the drop is subject to shear stress F_τ, viscous force F_μ and capillary forces acting tangentially on the surface of the liquid film at the contact lines. Under the lubrication approximation, the total shear force is $F_\tau = 2\tau R$. Based on velocity

https://doi.org/10.1017/jfm.2026.11746 Published online by Cambridge University Press

distribution (2.3*b*) (with slip length $\lambda = 0$), we have

$$\left.\frac{\partial u}{\partial z}\right|_{z=0} = \frac{\sigma}{\mu} h h''' + \frac{\tau}{\mu} = -\frac{\tau}{2\mu}. \tag{3.4}$$

Here, we have used the dimensional steady-state governing equation (3.2), which reads $hh''' + 3\tau/2\sigma = 0$. Thus the total viscous shear force induced by the substrate is

$$F_\mu = -2\mu R \left.\frac{\partial u}{\partial z}\right|_{z=0} = \tau R. \tag{3.5}$$

According to the horizontal force balance on the drop, we then arrive at

$$\sigma \cos(\theta_{up}\theta_e) - \sigma \cos(\theta_{down}\theta_e) = F_\tau + F_\mu = 3\tau R. \tag{3.6}$$

Equation (3.6) is consistent with the force analysis result by Dimitrakopoulos & Higdon (1997), who focused on the depinning condition of the drop under shear. Expanding (3.6) with respect to θ_e yields

$$\theta_{down}^2 - \theta_{up}^2 - 4S = 0. \tag{3.7}$$

The correctness of (3.7) is directly verified by the numerical results in figure 2, which shows that $\theta_{down}^2 - \theta_{up}^2$ grows linearly with S. At the threshold, we have $\theta_{up} = 0$ and hence the maximum downstream angle

$$\theta_{down} = 2\sqrt{S_{cr}}. \tag{3.8}$$

As θ_{up} vanishes at the threshold, the upstream-side asymptotic expansion for problem (3.2) and (3.3) has the following form:

$$H \sim \sqrt{\frac{8S}{3}} X^{\frac{3}{2}} + P_1 X^{\frac{5+\sqrt{13}}{4}} \quad \text{as} \quad X \to 0^+, \tag{3.9}$$

where P_1 is a free parameter to be determined in the numerical process. Interestingly, (3.9) is formally similar to the near-contact-line behaviour of a drop on a completely wetting substrate (Benilov & Benilov 2015). Moreover, asymptotic expansion (3.9) loses θ_{up} relative to (B3), because the upstream contact angle vanishes at the critical case. To restore a closed boundary-value problem, the critical shear number S_{cr} is treated as an additional unknown parameter. The resulting system is then solved simultaneously using the numerical algorithm described in Appendix B.2, yielding a precise value of the critical shear number $S_{cr} = 0.58857$. The corresponding drop profile at S_{cr} is shown in figure 2(*a*).

From another perspective, the volumetric flux for a pinned drop is

$$Q = \int_0^h u \mathrm{d}z = \frac{\sigma}{3\mu} h^3 h''' + \frac{\tau}{2\mu} h^2. \tag{3.10}$$

The steady state corresponds to $Q = 0$, implying that the shear-induced internal flow is exactly balanced by the capillary pressure gradient due to interface curvature. The critical shear number S_{cr} corresponds to the limit at which the drop can no longer generate a sufficient capillary pressure gradient to balance the shear-driven flux. In the present problem, this occurs when the upstream contact angle θ_{up} approaches zero.

The definition of the shear number S in (2.7) indicates an explicit relationship between the corresponding critical shear rate, drop size, surface tension, wettability and the viscosity of the displacing fluid. The present result shows that the critical shear rate is independent of the viscosity of the drop itself. Although the present model assumes a strictly pinned contact line corresponding to a 180° contact-angle hysteresis, experiments

https://doi.org/10.1017/jfm.2026.11746 Published online by Cambridge University Press

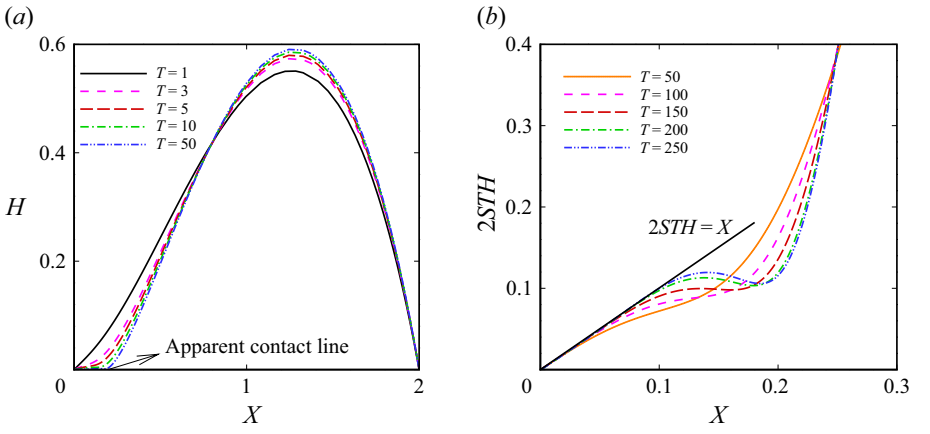


Figure 4. Unsteady evolution of a pinned drop under high shear $S = 1$: (*a*) drop profiles; (*b*) in the late stage of evolution ($T \gg 1$), a close-up view of the vanishing film region, with the height magnified by $2ST$.

on three-dimensional drops with finite hysteresis also show that the critical shear strength depends weakly on the drop viscosity (Fan *et al.* 2011; Xu *et al.* 2024).

3.2. *High shear: $S > S_{cr}$*

We take $S = 1 > S_{cr}$ as an example to explore the evolution of the pinned drop under high shear. As shown in figure 4(*a*), the drop near the upstream-side contact line gradually flattens, forming a thinning film with vanishing thickness. The main body of the drop evolves towards a quasi-steady shape, which connects to the thin film at an apparent contact line.

It is shown that the profile of the vanishing film becomes nearly straight in the late stage of the evolution, so that capillary force can be neglected in this region. Accordingly, the reduced governing equation and the corresponding asymptotic solution read

$$\frac{\partial H}{\partial T} + S\frac{\partial}{\partial X}\left(H^2\right) = 0 \Longrightarrow H \sim \frac{X}{2ST} \quad \text{as} \quad T \to \infty. \tag{3.11}$$

The accuracy of asymptotic solution (3.11) is confirmed in figure 4(*b*). Therefore, the thickness of the thin film continuously decreases but can never reach a steady state.

Figure 5 presents the temporal evolution of the microscopic contact angles on both sides of the drop. The upstream-side microscopic contact angle θ_{up} gradually decreases and asymptotically approaches zero, while the downstream-side contact angle θ_{down} increases and eventually reaches 1.898. Figure 5(*b*) also confirms the validity of asymptotic solution (3.11), according to which we have $\theta_{up} = 1/(2ST)$.

In the late stage of the evolution, almost all of the liquid is accumulated into the main body of the drop, which evolves in a quasi-steady manner. It can be shown that the main body of the drop is related to the critical steady solution developed above. The profile of the main body of the drop satisfies

$$HH''' + S = 0, \quad H(X_{cl}) = H'(X_{cl}) = H(2) = 0, \quad \int_{X_{cl}}^{2} H \,\mathrm{d}X = \frac{2}{3}, \tag{3.12}$$

where $X = X_{cl}$ denotes the position of the apparent contact line. Here, we have neglected the film thickness at the apparent contact line and imposed the vanishing slope condition

https://doi.org/10.1017/jfm.2026.11746 Published online by Cambridge University Press

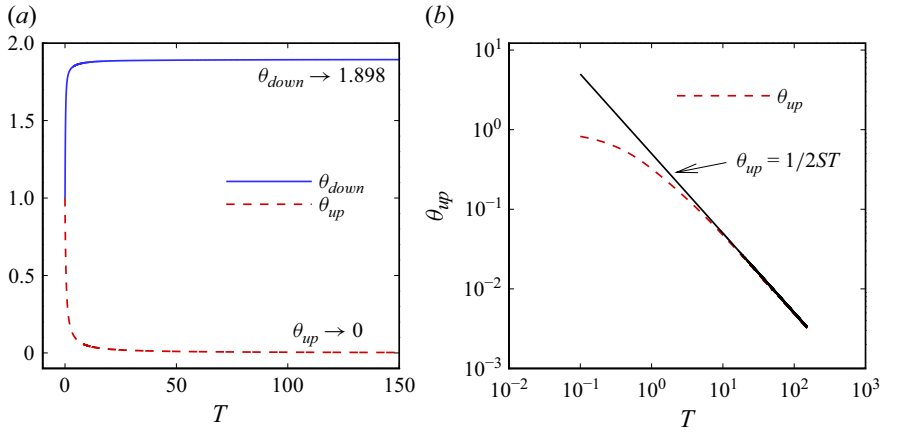


Figure 5. Unsteady evolution of a pinned drop under high shear $S = 1$: the variations of θ_{up} and θ_{down} with respect to the dimensionless time T.

since the main drop should conform to the thin film. Introducing the rescaling

$$X = \frac{2 - X_{cl}}{2}\tilde{X} + X_{cl}, \quad H = \frac{2}{2 - X_{cl}}\tilde{H}, \tag{3.13}$$

equation (3.12) is transformed into

$$\tilde{H}\tilde{H}''' + \left(\frac{2 - X_{cl}}{2}\right)^5 S = 0, \quad \tilde{H}(0) = \tilde{H}'(0) = \tilde{H}(2) = 0, \quad \int_0^2 \tilde{H}\,\mathrm{d}\tilde{X} = \frac{2}{3}, \tag{3.14}$$

which is formally equivalent to the steady problem (3.2) and (3.3) with S taken as S_{cr}. A comparison of the constant terms thus yields

$$X_{cl} = 2 - 2\left(\frac{S_{cr}}{S}\right)^{1/5}. \tag{3.15}$$

Furthermore, recalling that the critical downstream-side microscopic contact angle $\theta_{down} = 2\sqrt{S_{cr}}$ and using $H'(X) = (S/S_{cr})^{2/5}\tilde{H}'(\tilde{X})$, we obtain the late-stage downstream-side microscopic contact angle as

$$\theta_{down} = -H'(2) = 2S_{cr}^{1/10}S^{2/5}. \tag{3.16}$$

The theoretical predictions (3.15) and (3.16) agree well with the numerical results, as shown in figure 6.

As $T \to +\infty$, the local film profile near $X = X_{cl}$ develops a bending structure connecting the thin film and the main body of the drop. We show here that this local film profile has a vanishing size as $T \to \infty$ and is governed by a similarity solution, which can be obtained by introducing the ansatz

$$H(X, T) = \frac{X_{cl}}{2ST}\mathcal{H}(\xi), \quad \xi = S\left(\frac{2T}{X_{cl}}\right)^{\frac{2}{3}}(X - X_{cl}), \tag{3.17}$$

where $\mathcal{H}(\xi)$ is the similarity profile. Away from the apparent contact line, this structure should match the main body of the drop and the thinning film, which are described locally by $H \approx \sqrt{8S/3}(X - X_{cl})^{3/2}$ and $H \approx X_{cl}/(2ST)$ according to (3.9) and (3.11),

https://doi.org/10.1017/jfm.2026.11746 Published online by Cambridge University Press

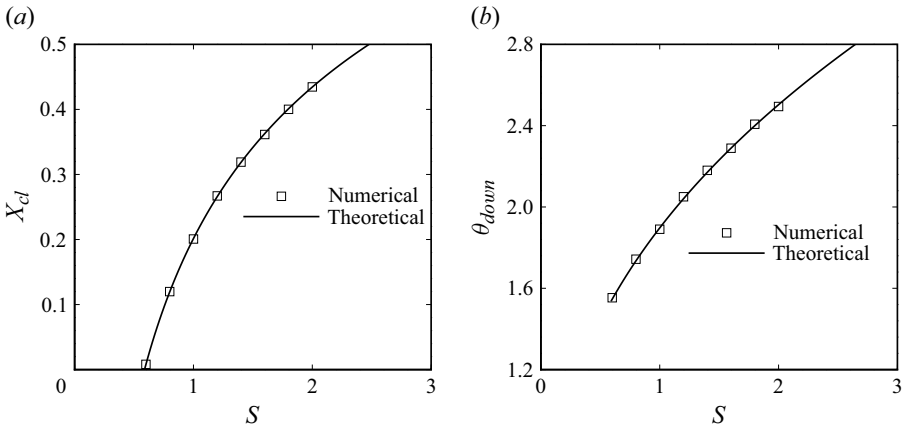


Figure 6. Late-stage behaviour of drop evolution under high shear: (*a*) theoretical prediction (3.15) and numerical results for X_{cl}; (*b*) theoretical prediction (3.16) and numerical results for the late-stage downstream-side microscopic contact angle θ_{down}.

respectively. For the similarity variables, these conditions become

$$\mathcal{H}(\xi) \sim \begin{cases} 1, & \text{as} \quad \xi \to -\infty, \\ \sqrt{\dfrac{8}{3}}\xi^{\frac{3}{2}}, & \text{as} \quad \xi \to +\infty. \end{cases} \tag{3.18}$$

After transformation (3.17), the time derivative term $\partial H/\partial T$ in the governing equation (2.12) is $O(T^{-2})$ and can be neglected compared with the remaining terms that are $O(T^{-4/3})$ as $T \to \infty$. Accordingly, after one integration, (2.12) reduces to

$$\mathcal{H}^3\mathcal{H}''' + \mathcal{H}^2 = 1, \tag{3.19}$$

where the integration constant is determined by the boundary condition as $\xi \to -\infty$. The boundary-value problem (3.18) and (3.19) can be conveniently solved using a shooting method. Figure 7 shows the similarity profile $\mathcal{H}(\xi)$ and compares it with the numerical results of the full problem at $S = 1$. In the late stage of the evolution, the profile of the capillary transition region gradually approaches the theoretical prediction. It is noteworthy that the calculation becomes increasingly challenging since the curvature near the apparent contact line, given by $\partial^2 H/\partial X^2 = S(2T/X_{cl})^{1/3}\mathcal{H}''(\xi)$, diverges as $T \to \infty$.

In summary, under the small-contact-angle assumption, when the shear number exceeds the critical value $S > S_{cr}$, the pinned state on the upstream side of the drop can be considered effectively lost, while the main body of the drop evolves in a quasi-steady manner. An idealised contact-angle hysteresis of 180° is adopted in the present study, thus, the critical shear for 'depinning' is linked to the condition that upstream contact angle goes to zero. However, for realistic drops with finite contact-angle hysteresis, depinning can occur earlier, either at the upstream or downstream side, depending on which contact angle first exceeds the hysteresis range. For drops with large contact angles, exceeding the critical shear leads to pinch-off and eventual detachment on the downstream side, which do not occur in the present work (Schleizer & Bonnecaze 1999; Spelt 2006; Ding & Spelt 2008; Ding *et al.* 2010).

https://doi.org/10.1017/jfm.2026.11746 Published online by Cambridge University Press

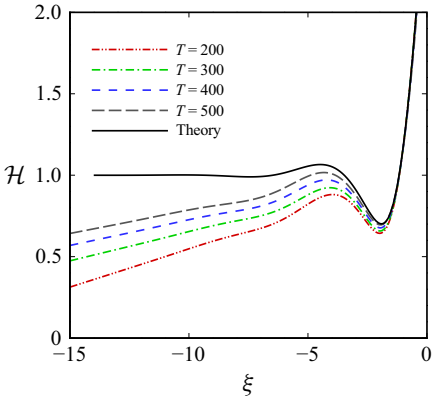


Figure 7. Profile of the capillary transition region connecting the vanishing film and main body in the late stage of unsteady drop evolution under high shear: comparison between the theoretical result (black line) and numerical profiles with $S = 1$.

4. Moving contact-line case: drop deformation and motion

In the presence of moving contact lines, the drop dynamics is governed by two dimensionless parameters, S and Λ. Numerical results confirm that a drop reaches a final steady state with a constant velocity c for any given shear number S. Focusing on the final steady states, we integrate governing equation (2.6) once to obtain

$$H(H+3\Lambda)H'''+S(H+2\Lambda)=c. \tag{4.1}$$

The corresponding boundary conditions, modified from (2.10), are

$$H(0)=H(L)=0,\ H'(0)=1,\ H'(L)=-1,\ \int_0^L H\,\mathrm{d}X=V=\frac{2}{3}, \tag{4.2}$$

where L denotes the undetermined drop length. Since L and c remain to be solved, we have added the mass conservation condition to close the problem.

Employing the numerical algorithm in Appendix A.2, the steady-state drop velocity c and length L for different S can be directly computed, as shown in figure 8. Drop motion dynamics with moving contact lines can be categorised into three regimes: low shear, intermediate shear and high shear. The division of the three regimes depends on the value of Λ. For example, for $\Lambda=10^{-5}$, the low-shear regime approximately corresponds to $S<0.5$, the intermediate-shear regime approximately corresponds to $0.5<S<0.62$ and the high-shear regime approximately corresponds to $S>0.62$.

In addition, starting from the steady-state governing equation (4.1), neglecting the slip-related small terms and integrating from 0 to L, we apply integration by parts together with the boundary conditions $H(0)=H(L)=0$ to obtain the following global balance relation:

$$VS=\int_0^L\left(-H'\right)^3\mathrm{d}X+cL. \tag{4.3}$$

Here, the left-hand side term VS represents the driving effect from the shear flow; the right-hand side terms $\int_0^L(-H')^3\mathrm{d}X$ and cL correspond to the capillary resistance effect and viscous resistance effect, respectively. Figure 9 shows the variation of the three terms with respect to S. There exists a critical turning point ($S=0.545$ for $\Lambda=10^{-5}$), beyond which the capillary resistance effect begins to decrease with S.

https://doi.org/10.1017/jfm.2026.11746 Published online by Cambridge University Press

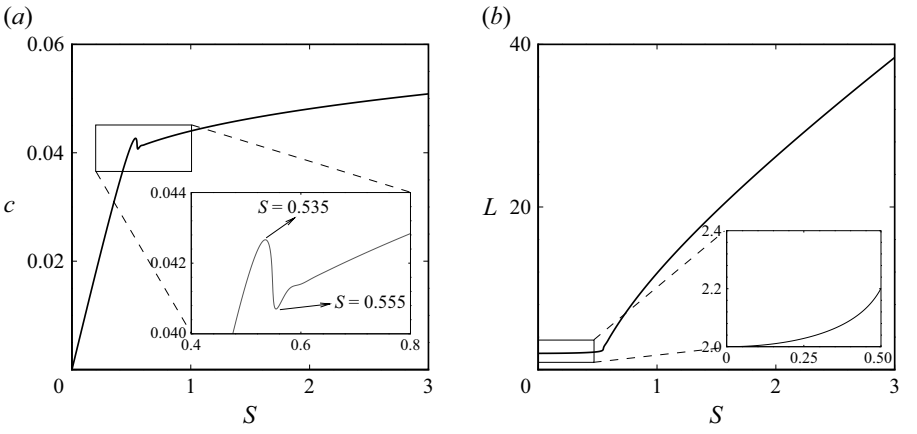


Figure 8. Variation of the steady-state drop (*a*) velocity c and (*b*) length L with respect to the increasing shear number S, with the slip $\Lambda = 10^{-5}$.

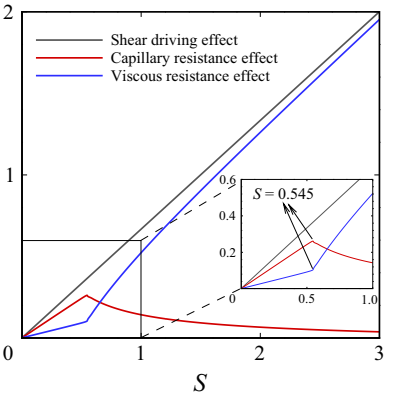


Figure 9. Variation of the steady-state shear-driven effect, capillary resistance effect and viscous resistance effect with respect to the shear number S, with the slip $\Lambda = 10^{-5}$.

4.1. *Low shear*

The drops under low shear are characterised by small velocity c, and an asymptotic theory can be developed following the procedure proposed by Hocking (1983), who considered the spreading of a thin drop in the absence or presence of gravity. For the present problem, the profile of the steady-state drop consists of an outer region and two inner regions near the advancing/receding contact lines.

In the outer region, the slip effect is insignificant, and thus the governing equation (4.1) reduces to

$$H^2 H''' + SH = c. \tag{4.4}$$

Considering that both the shear number S and the velocity c are small, we expand H to first order as

$$H = H_0 + cH_1 + SH_2 + O(c^2, S^2, cS), \tag{4.5}$$

https://doi.org/10.1017/jfm.2026.11746 Published online by Cambridge University Press

where H_0, H_1 and H_2 represent the static drop profile and the first-order corrections due to flow and shear, respectively. Substituting (4.5) into (4.4), we obtain

$$\begin{aligned} &H_0''' = 0, \quad H_0(0) = H_0(L) = 0, \quad \int_0^L H_0 \,\mathrm{d}X = V, \\ &H_1''' = \frac{1}{H_0^2}, \; H_1(0) = H_1(L) = 0, \; \int_0^L H_1 \mathrm{d}X = 0, \\ &H_2''' = -\frac{1}{H_0}, \; H_2(0) = H_2(L) = 0, \; \int_0^L H_2 \mathrm{d}X = 0. \end{aligned} \tag{4.6}$$

Solutions to (4.6) are

$$\begin{aligned} H_0 &= \frac{6V}{L^3} X(L - X), \\ H_1 &= \frac{L^3(L - X)X}{36V^2} \ln \frac{L - X}{X}, \\ H_2 &= \frac{L^2}{12V} \left[(L - X)^2 \ln \frac{L - X}{L} - X^2 \ln \frac{X}{L} \right]. \end{aligned} \tag{4.7}$$

It can be shown that the slope of the outer solution exhibits logarithmic singularities near the moving contact lines. Following Eggers (2005), for the purpose of matching, we provide the cube of the slope near the moving contact lines as

$$\left(H'_{out}\right)^3 \to \begin{cases} \left(\dfrac{6V}{L^2}\right)^3 - 9S\dfrac{V}{L} + 3c \ln \dfrac{L}{\mathrm{e}X}, & \text{for} \quad 0 < X \ll 1, \\ -\left(\dfrac{6V}{L^2}\right)^3 - 9S\dfrac{V}{L} + 3c \ln \dfrac{L}{\mathrm{e}(L - X)}, & \text{for} \quad 0 < L - x \ll 1. \end{cases} \tag{4.8}$$

The inner region is characterised by a length of Λ, over which a significant variation of the surface slope occurs due to the large viscous force therein. The analysis of (2.6) in the inner region reveals that the shear stress can be neglected near the contact line. Therefore, as shown in many previous studies (see, Hocking 1983; Eggers 2005; Benilov & Benilov 2015; Sibley *et al.* 2015; Savva, Rezgdanikov & Colinet 2017; Wang, Qin & Gao 2025), the inner solutions exhibits the following asymptotic behaviour in the far field:

$$\left(H'_{in}\right)^3 \to \begin{cases} 1 - 3c \ln \dfrac{\mathrm{e}X}{3\Lambda}, & \text{for} \quad \Lambda \ll X \ll 1, \\ -1 - 3c \ln \dfrac{\mathrm{e}(L - X)}{3\Lambda}, & \text{for} \quad \Lambda \ll L - X \ll 1. \end{cases} \tag{4.9}$$

A comparison of (4.8) and (4.9) shows that they can indeed match, yielding

$$3c \ln \frac{L}{3\Lambda} = 9S\frac{V}{L} - \left(\frac{6V}{L^2}\right)^3 + 1, \tag{4.10}$$

$$3c \ln \frac{L}{3\Lambda} = 9S\frac{V}{L} + \left(\frac{6V}{L^2}\right)^3 - 1. \tag{4.11}$$

https://doi.org/10.1017/jfm.2026.11746 Published online by Cambridge University Press

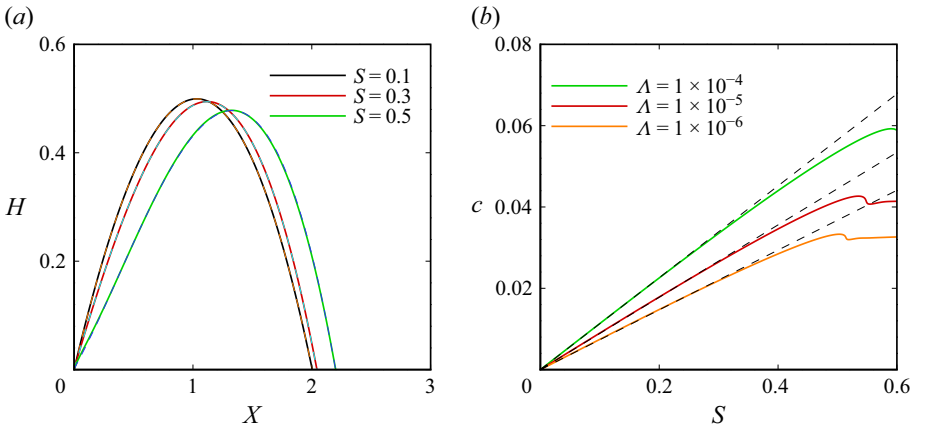


Figure 10. Steady-state drops under low shear: (*a*) numerical profiles (solid lines) and theoretical profiles (4.5) (dashed lines) for $S = 0.1,\ 0.3,\ 0.5$ and $\Lambda = 10^{-5}$ with the receding contact line shifted to $X = 0$, where the L in (4.5) comes from the numerical solutions; (*b*) comparison between the numerical velocities c (solid lines) and asymptotic predictions (4.12) (dashed lines) for slip lengths $\Lambda = 10^{-4},\ 10^{-5},\ 10^{-6}$.

Given $V = 2/3$, we finally obtain

$$L = 2, \quad c = \frac{S}{\ln \dfrac{2}{3\Lambda}}. \tag{4.12}$$

As exhibited in figure 10, the analytical results for the steady-state drop velocity c and drop profile $H(X)$ show good agreements with the numerical results in the low-shear regime. When S is small, the steady drop length L remains close to 2, and c is approximately proportional to S, with a proportionality coefficient given by $1/\ln(2/3\Lambda)$, as shown in figure 10(*b*). Ding *et al.* (2010) studied steadily moving drops in shear flow and reported that the drop speed increases linearly with shear rate in the low-Reynolds-number regime, consistent with the present predictions.

Asymptotic results (4.12) indicate that the drop essentially retains its original length in the low-shear regime. Although this prediction shows slight deviations from the numerical results in figure 8(*b*), the agreement remains reasonably good. Since the direction of shear (i.e. the sign of S) does not affect the drop length because of symmetry, a more refined theoretical description of L would require including higher-order even powers of S. Deriving these higher-order corrections involves considerably more algebraic complexity, and is beyond the scope of the present work.

Moreover, in the low-shear regime where the drop deformation is small and the drop profile remains close to the parabolic shape, the apparent contact angle θ_{ap} can be approximated by the interface slope of the leading-order outer solution evaluated at the contact line, i.e. $6V/L^2$. Under this approximation, the matching results (4.10) and (4.11) can be extended to the unsteady drop evolution and lead to the following Cox–Voinov-like law:

$$\theta_{ap,rec}^3 - 1 = -3c\ln\frac{L}{3\lambda} + 9S\frac{V}{L},\ \theta_{ap,adv}^3 - 1 = 3c\ln\frac{L}{3\lambda} - 9S\frac{V}{L}. \tag{4.13}$$

Equation (4.13) retains the characteristic cubic dependence of the Cox–Voinov law, with an effective macroscopic scale $L/3$ and microscopic scale λ, while the additional correction term $9SV/L$ reflects the influence of the external shear on the outer-region drop profile.

https://doi.org/10.1017/jfm.2026.11746 Published online by Cambridge University Press

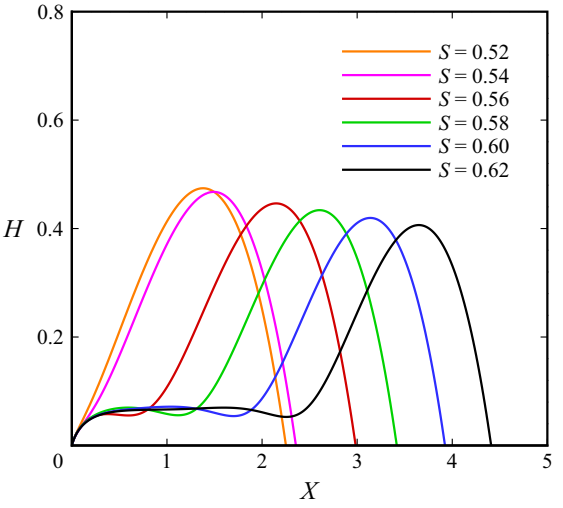


Figure 11. Steady-state drop profile under intermediate shear with $\Lambda = 10^{-5}$ and representative values of S. The receding contact line is shifted to $X = 0$.

4.2. *Intermediate shear*

Figure 11 shows that the drops under intermediate shear can no longer maintain the parabolic-like shape observed in the low-shear region. Instead, a flat film rapidly forms in the central region of the drop, and the drop length L experiences a sharp increase. Moreover, the non-dimensional time required for the drop to reach steady state increases by an order of magnitude.

As shown in figure 8(a), the steady-state velocity c of the drop exhibits a turning point at $S = 0.535$ (for $\Lambda = 10^{-5}$), where c begins to temporarily decrease despite increasing S. Comparing this with figure 9, we observe that, for $S = 0.535 < 0.545$, the shear driving effect, capillary resistance effect and viscous resistance effect still grow linearly with S, i.e. $cL \propto S$. Since the drop length L increases steeply with S in this regime, the increase in drop motion cost is slower than that of L, leading to a temporary decline in the drop speed c. Direct experimental measurements of drops under well-controlled constant shear are scarce. Nevertheless, qualitatively similar non-monotonic behaviour of the drop velocity has been reported in other configurations, i.e. gravity-driven drops on an inclined plane (Benilov & Benilov 2015) and drop motion on strained soft substrates (Chao, Jeon & Karpitschka 2025).

4.3. *High shear: steady-state profile*

In the high-shear regime, figure 12 shows the steady-state drop profiles at several representative shear numbers, illustrating the emergence of a pronounced flat film region in the drop rear. In the present study, the thin film effectively decouples the steady drop into three distinct zones: entrained film, dimple and capillary ridge. Similar elongation and structural features, including a thin trailing film, capillary ridge and the connecting dimple, have been observed qualitatively in experiments with moving drops (Fan *et al.* 2011; Wang *et al.* 2022; Xu *et al.* 2024).

4.3.1. *Entrained film*

The drop rear is characterised by the entrainment of thin film with a receding contact line. Its profile can also be determined via asymptotic analysis. We divide the drop rear region

https://doi.org/10.1017/jfm.2026.11746 Published online by Cambridge University Press

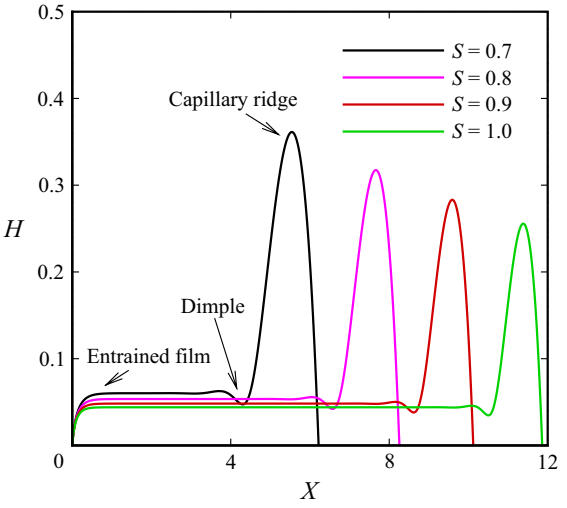


Figure 12. Steady-state drop profiles under high shear with $\Lambda = 10^{-5}$. The receding contact line is shifted to $X = 0$.

into an outer region and an inner region. In the outer region, the slip effect is insignificant and thus neglected, the reduced governing equation is again (4.4). The corresponding boundary conditions read

$$H(0) \to 0, \quad H(+\infty) \to \frac{c}{S}, \tag{4.14}$$

where the far-field film thickness can be easily obtained by neglecting the capillary force term in (4.4). Using the coordinate rescalings

$$H = \frac{c}{S}\bar{H}, \quad X = \frac{c^{2/3}}{S}\bar{X}, \tag{4.15}$$

we transform problem (4.4) and (4.14) into

$$\bar{H}^2\bar{H}''' + \bar{H} = 1, \quad \bar{H}(0) \to 0, \quad \bar{H}(+\infty) \to 1. \tag{4.16}$$

When $\bar{X} \to 0^+$, $\bar{H}$ has the following asymptotics:

$$\bar{H} \sim \bar{X}\left[-3\ln(k_0\bar{X})\right]^{1/3}. \tag{4.17}$$

We obtain $k_0 = 2.19$ by solving (4.16) with a shooting method and fitting the solution in the interval $\bar{X} \in [10^{-6}, 10^{-4}]$ to (4.17). Accordingly, we have

$$\left(H'_{out}\right)^3 \sim -3c\ln\frac{\mathrm{e}Sk_0X}{c^{2/3}}. \tag{4.18}$$

Matching (4.18) with the inner asymptotic behaviour in (4.9) yields the relation

$$c^{\frac{2}{3}}e^{-\frac{1}{3c}} = 3k_0\Lambda S \quad \Rightarrow \quad c = \frac{1}{2\mathscr{W}\left[\frac{1}{2}(3k_0\Lambda S)^{-3/2}\right]}, \tag{4.19}$$

https://doi.org/10.1017/jfm.2026.11746 Published online by Cambridge University Press

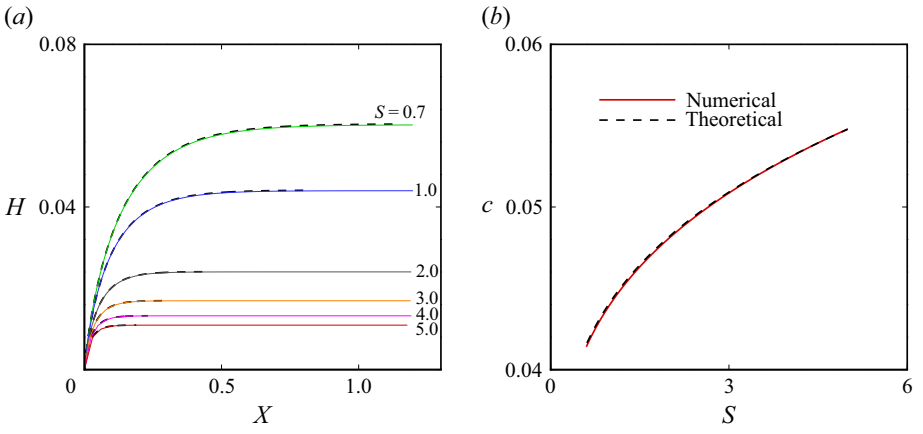


Figure 13. (*a*) Comparison between numerical profiles (solid lines) and shooting results (dashed lines) of the entrained film. (*b*) Comparison of steady-state drop velocity c as a function of S between numerical results (solid line) and theoretical prediction (4.19) (dashed line). The slip length $\Lambda = 10^{-5}$.

where $\mathscr{W}$ denotes the principal branch of the Lambert $\mathscr{W}$ function defined as the solution to $\mathscr{W}(x)e^{\mathscr{W}(x)} = x$ with $x > 0$, and admits the following asymptotic expansion:

$$\mathscr{W}(x) \sim \ln x - \ln\ln x + \frac{\ln\ln x}{\ln x} + \cdots, \quad \text{as} \quad x \to +\infty. \tag{4.20}$$

As shown in figure 13, both the drop rear profiles obtained via the shooting method and the steady velocity c predicted by (4.19) agree well with the numerical results.

4.3.2. *Capillary ridge*

For small drop velocity c, the capillary ridge is primarily determined by the balance between the capillary and shear forces. In what follows, we only compute the leading-order approximation of the drop height H in the capillary ridge region, omitting the effect of contact-line movement. For the macroscopic profile of the capillary ridge, the governing equation (4.1) reduces to

$$HH''' + S = 0, \tag{4.21}$$

which is the same as (3.2) for pinned drops.

For convenience, we shift the advancing contact line to $X = 0$, so that the right boundary condition reads

$$H(0) = 0. \tag{4.22}$$

Regarding the left-side boundary conditions, Benilov & Benilov (2015) and Wang *et al.* (2025) – in their studies on drop sliding and spin coating of liquid films – assumed that the capillary ridge approaches the X-axis with zero contact angle on the left. We adopt the same assumption here and neglect the thickness of the entrained film, as illustrated by the dashed line in figure 14(*b*). Thus, the left boundary conditions of (4.21) are prescribed as

$$H(-L_{ridge}) = 0, \quad H'(-L_{ridge}) = 0, \tag{4.23}$$

where L_{ridge} denotes the length of the capillary ridge.

It can be shown that the leading-order solution of the capillary ridge resembles the profile of a pinned drop under critical shear S_{cr}, as discussed in § 3.2. Supposing the

https://doi.org/10.1017/jfm.2026.11746 Published online by Cambridge University Press

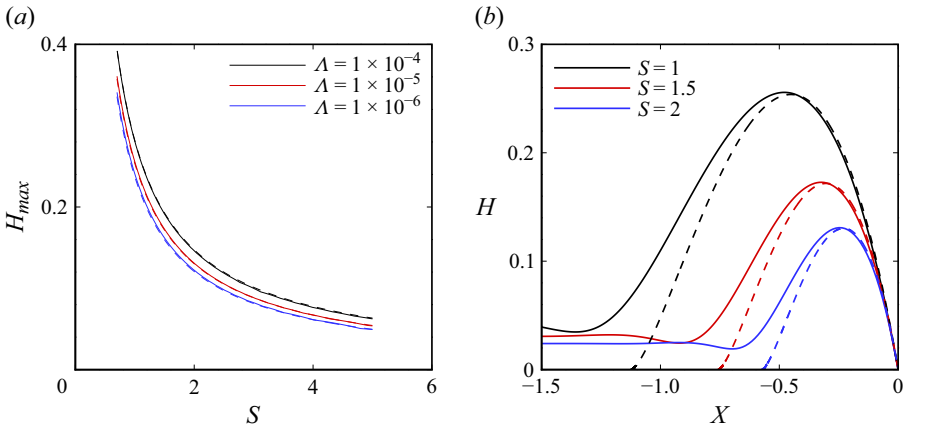


Figure 14. (*a*) Comparison between the leading-order prediction (4.30) with $\alpha = 20$ and numerical results for the maximum height of the capillary ridge. (*b*) Drop profile in the capillary ridge region with $\Lambda = 10^{-5}$: comparison between the leading-order outer solutions and the full numerical results. In both panels, dashed curves represent asymptotic results.

leading-order capillary ridge has a volume V_{ridge}, we introduce

$$X = \frac{L_{ridge}}{2}(\tilde{X} - 2), \quad H = \frac{3V_{ridge}}{L_{ridge}}\tilde{H}, \tag{4.24}$$

to transform problem (4.21)–(4.23) into

$$\tilde{H}\tilde{H}''' + \frac{L_{ridge}^5 S}{72V_{ridge}^2} = 0, \ \tilde{H}(0) = \tilde{H}(2) = 0, \ \tilde{H}'(0) = 0, \ \int_0^2 \tilde{H}\,\mathrm{d}\tilde{X} = \frac{2}{3}, \tag{4.25}$$

which is equivalent to the critical problem of pinned drops described by (3.2) and (3.3) with $S = S_{cr}$. A comparison of the constant terms yields

$$\frac{L_{ridge}^5 S}{72V_{ridge}^2} = S_{cr}. \tag{4.26}$$

To fully determine the solution, we still need a second relation between L_{ridge} and V_{ridge}, which turns out to be the apparent contact angle at the advancing contact line, $\theta_{ap} \equiv -H'(0)$. Strictly speaking, θ_{ap} should be determined by matching the macroscopic profile of the ridge to the inner solution near the advancing contact line. However, this approach is infeasible since even the leading-order problem (4.21) should be solved numerically. In the drop sliding problem driven by gravity, Benilov & Benilov (2015) studied the shape of the capillary ridge using empirically $\theta_{ap} = [1 + 3c\ln(1/\Lambda)]^{1/3}$, which, however, holds for the low-speed regime without film entrainment only. Instead, we introduce the Cox–Voinov relation $\theta_{ap} = [1 + 3c\ln(\alpha H_m/\Lambda)]^{1/3}$, where H_m is a macroscopic length and α is a fit parameter (Voinov 1976; Cox 1986). As suggested by Ming, Qin & Gao (2023), it is appropriate to take H_m to be the ridge height, which is approximately proportional to $1/S$, as shown below. Accordingly, we have

$$\theta_{ap} = \left(1 + 3c\ln\frac{\alpha}{S\Lambda}\right)^{\frac{1}{3}}, \tag{4.27}$$

https://doi.org/10.1017/jfm.2026.11746 Published online by Cambridge University Press

which further gives rise to

$$H'(0) = \frac{6V_{ridge}}{L_{ridge}^2}\tilde{H}'(2) = -\frac{12V_{ridge}}{L_{ridge}^2}\sqrt{S_{cr}} = -\left(1 + 3c\ln\frac{\alpha}{S\Lambda}\right)^{\frac{1}{3}}. \tag{4.28}$$

Here, we have used $\theta_{down} = -\tilde{H}'(2)$ given in (3.8).

Solving (4.26) and (4.28) simultaneously gives the leading-order predictions for L_{ridge} and V_{ridge} as

$$L_{ridge} = \frac{\left(1 + 3c\ln\frac{\alpha}{S\Lambda}\right)^{\frac{2}{3}}}{2S}, \quad V_{ridge} = \frac{\left(1 + 3c\ln\frac{\alpha}{S\Lambda}\right)^{\frac{5}{3}}}{48S^2\sqrt{S_{cr}}}. \tag{4.29}$$

The corresponding maximum height of the capillary ridge at leading order is

$$H_{max} = \frac{3V_{ridge}}{L_{ridge}}\tilde{H}_{max} = \frac{1 + 3c\ln\frac{\alpha}{S\Lambda}}{8S\sqrt{S_{cr}}}\tilde{H}_{max}, \tag{4.30}$$

where $\tilde{H}_{max} = 0.534$ can be inferred from figure 2. The maximum height H_{max} as a function of S is plotted in figure 14(a) for representative values of Λ. It can be seen that the numerical results agree perfectly with (4.30) with the fit parameter $\alpha = 20$. Figure 14(b) compares the leading-order ridge profiles with the numerical results and shows notable deviations in the upstream region, which are associated with the non-negligible thickness of the entrained film.

4.3.3. *Dimple*

Benilov *et al.* (2010) and Benilov & Benilov (2015) noted that, in similar gravity-driven drop motion problem, the dimple region may theoretically consist of an infinite hierarchy of asymptotic zones. Nonetheless, numerical solutions usually reveal only one or two discernible ripples, while the remaining structures are idealised mathematical constructs. Consequently, a detailed investigation of these higher-order features is beyond the scope of this study.

For the dimple region connecting the entrained film and capillary ridge, the governing equation remains the same as (4.4). Similar to the approach outlined in § 4.3.2, we assume the local film thickness is much smaller than the height of the capillary ridge. Away from the dimple, the film thickness approaches a constant c/S to the left and $\sqrt{8S/3}X^{(2/3)}$ to the right. Using the rescalings (4.15), we transform problem into

$$\bar{H}^2\bar{H}''' + \bar{H} = 1, \quad \bar{H}(-\infty) \to 1, \quad \bar{H}(+\infty) \to \sqrt{\frac{8}{3}}X^{\frac{2}{3}}. \tag{4.31}$$

Using the shooting method, we obtain the scaled dimple profile and compare it with the numerical solution, as shown in figure 15. It is seen that the numerical results of the full problem at different S values do collapse onto a single curve using the similarity variables (4.15). The similarity profile captures the oscillatory behaviours but shows large deviations, which are due to the fact that the thicknesses of the dimple and the capillary ridge are not well separated.

4.4. *High shear: unsteady evolution*

In the high-shear region, the drop exhibits interesting transient film structures before the final steady state is approached. Taking the case of $S = 1$ and $\Lambda = 10^{-5}$ as an example,

https://doi.org/10.1017/jfm.2026.11746 Published online by Cambridge University Press

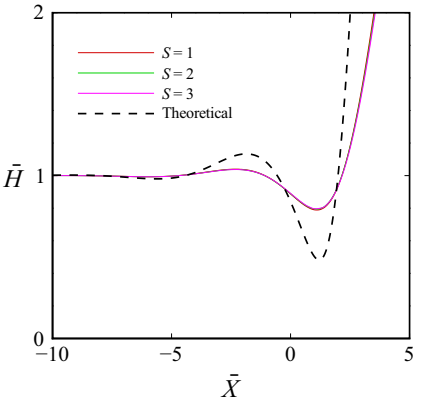


Figure 15. Comparison of the scaled dimple profiles between the numerical results and theoretical solution of problem (4.31), where the slip length is $\Lambda = 10^{-5}$.

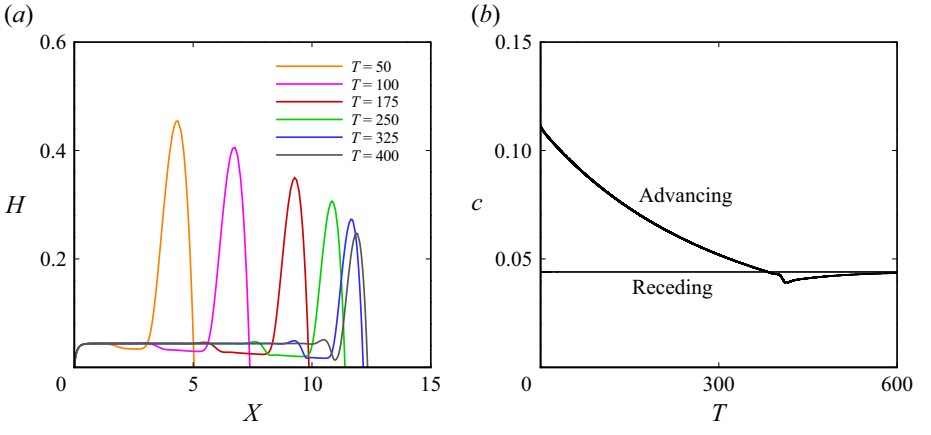


Figure 16. Unsteady evolution of a drop with $S = 1$ and $\Lambda = 10^{-5}$: (*a*) drop profiles with the receding contact lines shifted to $X = 0$; (*b*) time evolution of the advancing and receding contact-line velocities.

figure 16(*a*) shows the drop profiles at several times, while figure 16(*b*) presents the time evolution of the advancing and receding contact-line velocities. Throughout the evolution, the receding contact-line velocity remains approximately constant and equals the steady-state value, and the drop rear profile also remains unchanged. As the drop evolves, liquid is transported from the capillary ridge into the drop rear, resulting the elongation of the entrained film.

Additionally, we observe the emergence of an even thinner film near the capillary ridge, as shown in figure 16(*a*). The appearance of this thinner film bears resemblance to the classical thin films observed in dip-coating problems, where a liquid layer is entrained by withdrawing a solid plate from a bath, as first described by Landau & Levich (1942) and Derjaguin (1943). Similar thin-film structures have also been reported in studies of liquid entrainment associated with moving contact lines (Snoeijer *et al.* 2006; Gao *et al.* 2016; Xia, Qin & Gao 2020; Wang *et al.* 2025). Such thin films generated by liquid entrainment are known as Landau–Levich–Derjaguin (LLD) films, which scale with the 2/3 power of the local meniscus velocity relative to the substrate. By analogy, we interpret this thinner film as being entrained from the trailing edge of the capillary ridge through a similar

https://doi.org/10.1017/jfm.2026.11746 Published online by Cambridge University Press

mechanism, although its scaling with the meniscus velocity differs from the classical LLD law (as discussed later). Accordingly, we refer to it as an LLD-like film.

During the evolution, the length of LLD-like film first grows and then decreases. The LLD-like film eventually vanishes and evolves into the steady dimple structure discussed above, inducing a fluctuation in the advancing contact-line velocity at roughly $T = 400$, as shown in figure 16(*b*). Interestingly, the LLD-like film is characterised by a non-uniform thickness, while the profiles remain approximately aligned along the same line throughout its evolution. These findings suggest that the film is produced through the local dynamics; once generated, the film itself hardly varies with time.

To estimate the thickness of the LLD-like film, we focus on the dynamic meniscus connecting the LLD-like film and the capillary ridge. Since the capillary ridge varies slowly in time (i.e. in a quasi-steady state), the dynamic meniscus can therefore be regarded as moving with the advancing contact-line speed c_{adv}. As mentioned before, the liquid is transported from the capillary ridge into the drop rear, which implies that the flux through the dynamic meniscus cannot be neglected. In a reference frame comoving with the meniscus, the local film is approximately steady and governed by

$$H^3 H''' + S(H^2 - H_L^2) = c_{adv}(H - H_L), \tag{4.32}$$

where H_L denotes the thickness of the LLD-like film with its weak non-uniformity neglected.

Since the thickness of the LLD-like film is small compared with that of the ridge, we can also assume that the capillary ridge contacts the substrate at the left end with a zero contact angle. Therefore, similar to § 4.3.3, the right-side far-field boundary condition of the dynamic meniscus reads $H \to \sqrt{8S/3}X^{3/2}$. The left end of the dynamic meniscus connects to the flat LLD-like film, leading to the left-side far-field boundary condition $H \to H_L$.

We introduce $H = H_L\bar{H}$ and $X = H_L\bar{X}/c_{adv}^{1/3}$ to transform (4.32) and the corresponding boundary conditions into

$$\bar{H}^3\bar{H}''' + K(\bar{H}^2 - 1) = \bar{H} - 1, \quad \bar{H} \sim \begin{cases} 1, & \text{as} \quad \bar{X} \to -\infty, \\ \sqrt{\dfrac{8K}{3}}\bar{X}^{\frac{3}{2}}, & \text{as} \quad \bar{X} \to +\infty, \end{cases} \tag{4.33}$$

where $K = SH_L/c_{adv}$.

Problem (4.33) is solved using the shooting method. In particular, we determine $K = 0.2234$, and hence

$$H_L = 0.2234\,\frac{c_{adv}}{S}. \tag{4.34}$$

This relation implies that the thickness of the LLD-like film is proportional to the advancing contact-line velocity c_{adv} and inversely proportional to the shear number S, which differs from the classical LLD law. As shown in figure 17, a better agreement with numerical results is achieved when the coefficient is modified as $K = 0.36$. We attribute this deviation to the approximations made in the theoretical derivation. For instance, the height of the capillary ridge is not significantly larger than the thickness of the LLD-like film (only approximately $13 \sim 17$ times greater), which violates the assumption of clear scale separation.

https://doi.org/10.1017/jfm.2026.11746 Published online by Cambridge University Press

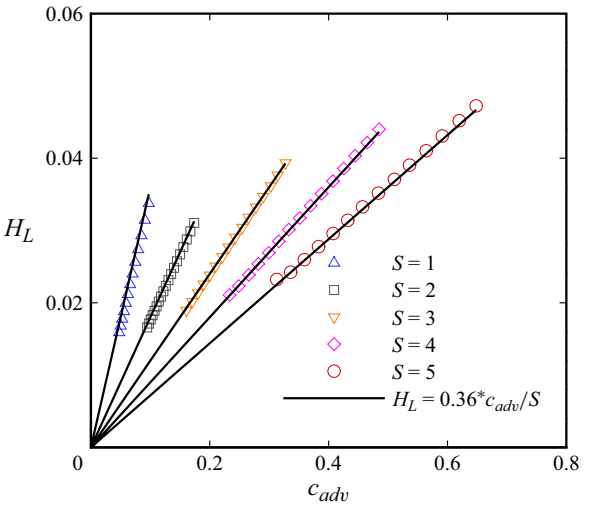


Figure 17. Comparison of LLD-like film thickness with the asymptotic theory $H_L = 0.36 c_{adv}/S$ with $\Lambda = 10^{-5}$.

5. Conclusions

We have conducted a numerical and theoretical investigation into the deformation and motion of the two-dimensional thin drops in a shear flow, considering both pinned and moving contact-line conditions.

For drops with pinned contact lines, we identify a critical shear number $S_{cr} = 0.58857$, beyond which the upstream side becomes unstable and a thinning film develops. The critical shear rate is controlled by the drop size, surface tension, wettability and the viscosity of the displacing fluid, while being independent of the drop viscosity, in qualitative agreement with the theoretical prediction of Dussan (1987). In the late stage of drop evolution with $S > S_{cr}$, the upstream side of the drop degenerates into a thin film whose slope scales as $1/T$. This thin film is connected to the quasi-steady main body of the drop through a capillary transition structure, which is described by a self-similar solution. It is therefore evident that the behaviour of small-contact-angle drops at $S > S_{cr}$ differs from that of large-contact-angle drops, the latter undergoing strong deformation and eventually exhibiting detachment.

For drops with moving contact lines, the dynamical behaviours can be classified into three regimes according to the shear strength. In the low-shear region, the drop rapidly reaches a steady state. The drop steady-state profile can be well described by a leading-order approximation, and the steady-state velocity increases linearly with the shear number S. In the intermediate-shear region, the steady drop shape no longer maintains a parabolic-like shape. Instead, a significant deformation of the drop occurs, characterised by a non-monotonic variation of the drop velocity with the shear number S. In the high-shear region, the steady-state drop profile can be clearly divided into three distinct regions: entrained film, dimple and capillary ridge. Moreover, during the drop evolution, an LLD-like film emerges immediately adjacent to the capillary ridge. The thickness of this LLD-like film is found to be proportional to the meniscus velocity c (also the advancing contact-line velocity), which differs from the classical $c^{2/3}$ LLD law (Landau & Levich 1942; Derjaguin 1943).

Funding. This work was supported by the NSFC (grant nos. 12388101, 12241204 and 12325208) and China Postdoctoral Science Foundation (grant no. 2025M781801).

https://doi.org/10.1017/jfm.2026.11746 Published online by Cambridge University Press

Declarations of interests. The authors report no conflict of interest.

Appendix A. Numerical method for moving contact lines

A.1. *Unsteady evolution of the drops: problem (2.6), (2.8)–(2.11)*

For numerically solving the boundary-value problem (2.6), (2.8)–(2.11), the main difficulty results from the fact that (2.6) is singular at both boundaries, indicating a diverging H_{XXX} at the contact lines. Physically, this is because the Navier-slip model removes the singularity in the velocity gradient but fails to regularise the divergence in the pressure gradient at the contact lines (Buckingham, Shearer & Bertozzi 2003; Snoeijer & Andreotti 2013). Therefore, we apply a small truncation of ϵ at both the advancing and receding contact lines to avoid the diverging H_{XXX}, so that the computational domain is truncated to $[L_{rec}+\epsilon,\, L_{adv}-\epsilon]$. Furthermore, the time-dependent domain $X\in[L_{rec}+\epsilon,\, L_{adv}-\epsilon]$ is transformed into the fixed domain $Y\in[0,\,1]$ after the mapping

$$X = L_{rec}+\epsilon+LY,\ \ L = L_{adv}-L_{rec}-2\epsilon. \tag{A1}$$

Accordingly,

$$\frac{\partial}{\partial X}=\frac{1}{L}\frac{\partial}{\partial Y},\qquad \left.\frac{\partial}{\partial T}\right|_X=\left.\frac{\partial}{\partial T}\right|_Y-\frac{c_{rec}+(c_{adv}-c_{rec})Y}{L}\frac{\partial}{\partial Y}, \tag{A2}$$

and then the governing equation (2.6) becomes

$$\frac{\partial H}{\partial T}-\frac{c_{rec}+(c_{adv}-c_{rec})Y}{L}\frac{\partial H}{\partial Y}+\frac{1}{L^4}\frac{\partial}{\partial Y}\left[H^2(H+3\Lambda)\frac{\partial^3 H}{\partial Y^3}\right]+\frac{S}{L}\frac{\partial}{\partial Y}\left[H(H+2\Lambda)\right]=0. \tag{A3}$$

We discretise the time derivative $\partial H/\partial T$ using an implicit backward Euler scheme, while treating the contact-line velocities c_{rec} and c_{adv} explicitly via forward differences

$$\left(\frac{\partial H}{\partial T}\right)^n=\frac{H^n-H^{n-1}}{\Delta T},\ c_{rec}^{n-1}=\frac{L_{rec}^n-L_{rec}^{n-1}}{\Delta T},\ c_{adv}^{n-1}=\frac{L_{adv}^n-L_{adv}^{n-1}}{\Delta T}, \tag{A4}$$

where the superscripts n and $n-1$ denote quantities at times T and $T-\Delta T$, respectively. As a result, at the current time step T^n, the drop length L is explicitly given as

$$L^n=L_{adv}^n-L_{rec}^n-2\epsilon=\Delta T\,(c_{adv}^{n-1}-c_{rec}^{n-1})+L_{adv}^{n-1}-L_{rec}^{n-1}-2\epsilon=\Delta T\,(c_{adv}^{n-1}-c_{rec}^{n-1})+L^{n-1}. \tag{A5}$$

Appropriate boundary conditions should be imposed at the new boundaries. Following Benilov & Benilov (2015) and Wang *et al.* (2025), we adopt the boundary expansions for governing equation (2.6) within conditions (2.11)

$$H=\begin{cases}\chi_r+\left(\dfrac{c_{rec}}{6\Lambda}-\dfrac{S}{3}\right)\chi_r^2\ln\chi_r+P_1\chi_r^2+O\left(\chi_r^3\ln\chi_r\right), & \text{as}\quad \chi_r=X-L_{rec}\to 0^+,\\ \chi_a-\left(\dfrac{c_{adv}}{6\Lambda}-\dfrac{S}{3}\right)\chi_a^2\ln\chi_a+P_2\chi_a^2+O\left(\chi_a^3\ln\chi_a\right), & \text{as}\quad \chi_a=L_{adv}-X\to 0^+,\end{cases} \tag{A6}$$

where P_1, P_2 are the free parameters to be determined. For the fourth-order equation (A3), the determination of the unknown boundary parameters P_1, P_2 and the contact-line velocities c_{rec}, c_{adv} requires eight boundary conditions. Therefore, we evaluate the values of H and its first three derivatives at $Y=0$ and 1 from expansions (A6), respectively, yielding eight boundary conditions to close the problem.

https://doi.org/10.1017/jfm.2026.11746 Published online by Cambridge University Press

The initial conditions are given by

$$L_{rec}=0,\ L_{adv}=2,\ P_1=P_2=0,\ c_{rec}=c_{adv}=0,\ H_{init}=X-X^2/2. \tag{A7}$$

At each time step, we use bvp5c in MATLAB, which employs an adaptive mesh strategy to handle the stiffness of the problem, to solve this boundary-value problem. Accuracy of the numerical method is controlled by adjusting the absolute and relative error tolerances, time step ΔT and cutoff parameter ϵ, all of which are chosen to be sufficiently small so that no visible differences appear in the numerical results. Numerical results indicate that the cutoff position yields convergent results when $\epsilon=\Lambda/10$, consistent with Benilov & Benilov (2015). Accordingly, we take $\epsilon=\Lambda/10$ and $\Delta T=0.01$ for all the numerical results in this paper. This set-up maintains liquid volume conservation to within 0.1 % over the entire drop motion process.

A.2. *Steady states of the drops: problem (4.1)–(4.2)*

A small truncation of ϵ at both the advancing and receding contact lines is also introduced. We transform the computational domain $X\in[\epsilon,\ L-\epsilon]$ into the fixed domain $Y\in[0,\ 1]$ using the mapping $X=\epsilon+(L-2\epsilon)Y$. Accordingly, the governing equation (4.1) becomes

$$\frac{H(H+3\Lambda)}{(L-2\epsilon)^3}\frac{\mathrm{d}^3H}{\mathrm{d}Y^3}+S(H+2\Lambda)=c. \tag{A8}$$

Similar to (A6), the boundary expansions for governing equation (4.1) within conditions (4.2) reduce to

$$H=\begin{cases}\chi_r+\left(\dfrac{c}{6\Lambda}-\dfrac{S}{3}\right)\chi_r^2\ln\chi_r+P_1\chi_r^2+O\left(\chi_r^3\ln\chi_r\right), & \text{as}\quad \chi_r=X\to 0^+,\\ \chi_a-\left(\dfrac{c}{6\Lambda}-\dfrac{S}{3}\right)\chi_a^2\ln\chi_a+P_2\chi_a^2+O\left(\chi_a^3\ln\chi_a\right), & \text{as}\quad \chi_a=L-X\to 0^+.\end{cases} \tag{A9}$$

To enforce the mass conservation condition, we introduce an auxiliary function $M'=H$, with integral boundary conditions $M(0)=0$ and $M(L)=2/3$.

For the third-order equation (A8) and auxiliary function $M'=H$, the determination of the unknown boundary parameters P_1 and P_2, the drop length L and the drop velocity c requires eight boundary conditions. These are provided by evaluating H and its first and second derivatives at $Y=0$ and $Y=1$ from the expansions (A9), together with the integral boundary conditions. In practice, we obtain the steady profiles of the drops by sweeping over the shear number S, increasing it by $\Delta S=0.001$ at each step, and using the solution from the previous step as the initial guess for the next computation.

Appendix B. Numerical method for pinned contact lines

B.1. *Unsteady evolution of the drops: problem (2.12)–(2.13)*

As mentioned in § 2.2, for governing equation (2.12), pressure gradient (associated with H_{XXX}) is singular at the contact lines, which necessitates introducing a small truncation ϵ at both the upstream and downstream contact lines. Asymptotic expansions near the pinned contact lines must account for the time variations of the microscopic contact angles (Bernis *et al.* 2000; Eggers & Fontelos 2025). Consequently, we give the asymptotic expansions

https://doi.org/10.1017/jfm.2026.11746 Published online by Cambridge University Press

of H near the pinned contact lines as

$$H=\begin{cases}\theta_{up}X-\left(\dfrac{S}{2\theta_{up}}+\dfrac{\dot{\theta}_{up}}{4\theta_{up}^3}\right)X^2\ln X+P_1X^2+O(X^3\ln X), & \text{as } X\to 0^+,\\ \theta_{down}(2-X)+\left(\dfrac{S}{2\theta_{down}}-\dfrac{\dot{\theta}_{down}}{4\theta_{down}^3}\right)(2-X)^2\ln(2-X)+P_2(2-X)^2+O[(2-X)^3\ln(2-X)], & \text{as } X\to 2^-.\end{cases}\tag{B1}$$

When $S=0$, asymptotic expansion (B1) reduces to the form given by Eggers & Fontelos (2025).

For the fourth-order differential equation (2.12), the determination of the unknown boundary parameters P_1, P_2 and microscopic contact angles θ_{up}, θ_{down} requires eight boundary conditions. We evaluate the values of H and its first three derivatives at $X=\epsilon$ and $2-\epsilon$ from expansion (B1), respectively, yielding eight boundary conditions to close the problem.

For the time discretisation, we adopt an implicit backward Euler scheme for $\partial H/\partial T$, $\dot{\theta}_{up}$ and $\dot{\theta}_{down}$, i.e.

$$\left(\frac{\partial H}{\partial T}\right)^n=\frac{H^n-H^{n-1}}{\Delta T},\ \dot{\theta}_{up}^n=\frac{\theta_{up}^n-\theta_{up}^{n-1}}{\Delta T},\ \dot{\theta}_{down}^n=\frac{\theta_{down}^n-\theta_{down}^{n-1}}{\Delta T}.\tag{B2}$$

Similar to Appendix A.1, the relevant parameters are set to $\epsilon=10^{-6}$ and $\Delta T=0.01$.

B.2. *Steady states of the drops: problem (3.2)–(3.3)*

A small truncation of $\epsilon=1\mathrm{e}-6$ at both the upstream and downstream contact lines is also introduced here.

For the steady-state problem (3.2)–(3.3) with $S<S_{cr}$, asymptotic expansion (B1) reduces to

$$H=\begin{cases}\theta_{up}X-\dfrac{S}{2\theta_{up}}X^2\ln X+P_1X^2+O(X^3\ln X), & \text{as } X\to 0^+,\\ \theta_{down}(2-X)+\dfrac{S}{2\theta_{down}}(2-X)^2\ln(2-X)+P_2(2-X)^2+O[(2-X)^3\ln(2-X)], & \text{as } X\to 2^-.\end{cases}\tag{B3}$$

Similar to Appendix A.2, the volume conservation is imposed by introducing an auxiliary function $M'=H$. For the third-order differential equation (3.2) and auxiliary function $M'=H$, the determination of the unknown boundary parameters P_1, P_2 and microscopic contact angles θ_{up}, θ_{down} requires eight boundary conditions. These are provided by evaluating H and its first and second derivatives at $X=\epsilon$ and $X=2-\epsilon$ from the asymptotic expansions (B3), together with the integral boundary conditions $M(\epsilon)=0$ and $M(2-\epsilon)=2/3$.

As mentioned in § 3.1, for the steady-state critical problem (3.2), (3.3) with $S=S_{cr}$, the zero upstream-side microscopic contact angle implies that the upstream-side asymptotic expansion in (B3) should be modified to expansion (3.9). Since expansion (3.9) lacks the boundary parameter θ_{up}, it contains one fewer unknown boundary coefficients than expansion (B3). Consequently, the critical shear number S_{cr} can be introduced as an additional unknown parameter to be determined.

Specific details are omitted here, as they have been thoroughly presented and referenced in the previous appendices.

https://doi.org/10.1017/jfm.2026.11746 Published online by Cambridge University Press

References

Ahmadlouydarab, M. & Feng, J.J. 2014 Motion and coalescence of sessile drops driven by substrate wetting gradient and external flow. *J. Fluid Mech.* **746**, 214–235.

Andreotti, B. & Snoeijer, J.H. 2020 Statics and dynamics of soft wetting. *Annu. Rev. Fluid Mech.* **52** (1), 285–308.

Benilov, E.S. & Benilov, M.S. 2015 A thin drop sliding down an inclined plate. *J. Fluid Mech.* **773**, 75–102.

Benilov, E.S., Chapman, S.J., McLeod, J.B., Ockendon, J.R. & Zubkov, V.S. 2010 On liquid films on an inclined plate. *J. Fluid Mech.* **663**, 53–69.

Bernis, F., Hulshof, J. & King, A.C. 2000 Dipoles and similarity solutions of the thin film equation in the half-line. *Nonlinearity* **13** (2), 413–439.

Bonn, D., Eggers, J., Indekeu, J., Meunier, J. & Rolley, E. 2009 Wetting and spreading. *Rev. Mod. Phys.* **81**, 739–805.

Buckingham, R., Shearer, M. & Bertozzi, A. 2003 Thin film traveling waves and the Navier slip condition. *SIAM J. Appl. Math.* **63** (2), 722–744.

Castrejón-Pita, J.R., Muñoz-Sánchez, B.N., Hutchings, I.M. & Castrejón-Pita, A.A. 2016 Droplet impact onto moving liquids. *J. Fluid Mech.* **809**, 716–725.

Chao, Y., Jeon, H. & Karpitschka, S. 2025 Nonmonotonic motion of sliding droplets on strained soft solids. *Phys. Rev. Lett.* **134** (18), 184001.

Cox, R.G. 1986 The dynamics of the spreading of liquids on a solid surface. Part 1. Viscous flow. *J. Fluid Mech.* **168**, 169–194.

Derjaguin, B.V. 1943 Thickness of liquid layer adhering to walls of vessels on their emptying. *Acta Physicochim. URSS* **20**, 349–352.

Dimitrakopoulos, P. 2007a Deformation of a droplet adhering to a solid surface in shear flow: onset of interfacial sliding. *J. Fluid Mech.* **580**, 451–466.

Dimitrakopoulos, P. 2007b Gravitational effects on the deformation of a droplet adhering to a horizontal solid surface in shear flow. *Phys. Fluids* **19**, 122105.

Dimitrakopoulos, P. & Higdon, J.J.L. 1997 Displacement of fluid droplets from solid surfaces in low-Reynolds-number shear flows. *J. Fluid Mech.* **336**, 351–378.

Dimitrakopoulos, P. & Higdon, J.J.L. 1998 On the displacement of three-dimensional fluid droplets from solid surfaces in low-Reynolds-number shear flows. *J. Fluid Mech.* **377**, 189–222.

Ding, H., Gilani, M.N.H. & Spelt, P.D.M. 2010 Sliding, pinch-off and detachment of a droplet on a wall in shear flow. *J. Fluid Mech.* **644**, 217–244.

Ding, H. & Spelt, P.D.M. 2008 Onset of motion of a three-dimensional droplet on a wall in shear flow at moderate Reynolds numbers. *J. Fluid Mech.* **599**, 341–362.

Durbin, P.A. 1988 On the wind force needed to dislodge a drop adhered to a surface. *J. Fluid Mech.* **196**, 205–222.

Dussan, V.E.B. 1987 On the ability of drops to stick to surfaces of solids. Part 3. The influences of the motion of the surrounding fluid on dislodging drops. *J. Fluid Mech.* **3–174**, 381–397.

Dussan, V.E.B. & Davis, S.H. 1974 On the motion of a fluid–fluid interface along a solid surface. *J. Fluid Mech.* **65**, 71–95.

Eggers, J. 2005 Existence of receding and advancing contact lines. *Phys. Fluids* **17** (8), 082106.

Eggers, J. & Fontelos, M.A. 2025 Dynamics of a film bounded by a pinned contact line. *J. Fluid. Mech.* **1008**, A47.

Fan, J., Wilson, M.C.T. & Kapur, N. 2011 Displacement of liquid droplets on a surface by a shearing air flow. *J. Colloid Interface Sci.* **356** (1), 286–292.

Gao, P., Li, L., Feng, J.J., Ding, H. & Lu, X.Y. 2016 Film deposition and transition on a partially wetting plate in dip coating. *J. Fluid Mech.* **791**, 358–383.

Gupta, A. & Sbragaglia, M. 2014 Deformation and breakup of viscoelastic droplets in confined shear flow. *Phys. Rev. E* **90** (2), 023305.

Hocking, L.M. 1983 The spreading of a thin drop by gravity and capillarity. *Q. J. Mech. Appl. Math.* **36** (1), 55–69.

Hooshanginejad, A. & Lee, S. 2022 Dynamics of a partially wetting droplet under wind and gravity. *Phys. Rev. Fluids* **7** (3), 033601.

Huh, C. & Scriven, L.E. 1971 Hydrodynamic model of steady movement of a solid/liquid/fluid contact line. *J. Colloid Interface Sci.* **35** (1), 85–101.

Huppert, H.E. 1982 Flow and instability of a viscous current down a slope. *Nature* **300** (5891), 427–429.

Kang, D., Nadim, A. & Chugunova, M. 2016 Dynamics and equilibria of thin viscous coating films on a rotating sphere. *J. Fluid Mech.* **791**, 495–518.

https://doi.org/10.1017/jfm.2026.11746 Published online by Cambridge University Press

LANDAU, L.D. & LEVICH, B.V. 1942 Dragging of a liquid by a moving plate. *Acta Physicochim. URSS* **17**, 42–54.
LI, X. & POZRIKIDIS, C. 1996 Shear flow over a liquid drop adhering to a solid surface. *J. Fluid Mech.* **307**, 167–190.
LIU, H., ZHANG, J., BA, Y., WANG, N. & WU, L. 2020 Modelling a surfactant-covered droplet on a solid surface in three-dimensional shear flow. *J. Fluid Mech.* **897**, A33.
LOHSE, D. 2022 Fundamental fluid dynamics challenges in inkjet printing. *Annu. Rev. Fluid Mech.* **54** (1), 349–382.
LU, H., XU, X., XIE, L.S., WANG, H.L., SUN, G.N. & YANG, Q. 2019 Deformation and crawling of oil drop on solid substrates by shearing liquid. *Chem. Engng Sci.* **195**, 720–729.
MADANI, S. & AMIRFAZLI, A. 2014 Oil drop shedding from solid substrates by a shearing liquid. *Colloids Surf. A Physicochem. Engng Asp.* **441**, 796–806.
MHATRE, N.V. & KUMAR, S. 2024 Shear-induced depinning of thin droplets on rough substrates. *J. Fluid Mech.* **990**, A14.
MING, H., QIN, J. & GAO, P. 2023 Early stage of bubble spreading in a viscous ambient liquid. *J. Fluid Mech.* **964**, A41.
MORTAZAVI, M. & JUNG, S.Y. 2023 Role of droplet dynamics on contact line depinning in shearing gas flow. *Langmuir* **39** (30), 10301–10311.
ORON, A., DAVIS, S.H. & BANKOFF, S.G. 1997 Long-scale evolution of thin liquid films. *Rev. Mod. Phys.* **69** (3), 931–980.
PAN, Y., WANG, Z.B., ZHAO, X.Y., DENG, W.W. & XIA, H.H. 2022 On axisymmetric dynamic spin coating with a single drop of ethanol. *J. Fluid Mech.* **951**, A30.
QIN, J. & GAO, P. 2018 Asymptotic theory of fluid entrainment in dip coating. *J. Fluid Mech.* **844**, 1026–1037.
QIN, J., LU, W. & GAO, P. 2024 A numerical method for dynamic wetting using mesoscopic contact-line models. *Commun. Comput. Phys.* **36**, 977–995.
SAVVA, N., GROVES, D. & KALLIADASIS, S. 2019 Droplet dynamics on chemically heterogeneous substrates. *J. Fluid Mech.* **859**, 321–361.
SAVVA, N., REZGDANIKOV, A. & COLINET, P. 2017 Asymptotic analysis of the evaporation dynamics of partially wetting droplets. *J. Fluid Mech.* **824**, 574–623.
SCHLEIZER, A.D. & BONNECAZE, R.T. 1999 Displacement of a two-dimensional immiscible droplet adhering to a wall in shear and pressure-driven flows. *J. Fluid Mech.* **383**, 29–54.
SEEVARATNAM, G.K., DING, H., MICHEL, O., HENG, J.Y.Y. & MATAR, O.K. 2010 Laminar flow deformation of a droplet adhering to a wall in a channel. *Chem. Engng Sci.* **65** (16), 4523–4534.
SHANG, X., LUO, Z., HU, G. & BAI, B. 2022 Role of surfactant-induced Marangoni effects in droplet dynamics on a solid surface in shear flow, colloids surf. *Colloids Surf. A Physicochem. Engng Asp.* **654**, 130142.
SIBLEY, D.N., NOLD, A. & KALLIADASIS, S. 2015 The asymptotics of the moving contact line: cracking an old nut. *J. Fluid Mech.* **764**, 445–462.
SNOEIJER, J.H. & ANDREOTTI, B. 2013 Moving contact lines: scales, regimes, and dynamical transitions. *Annu. Rev. Fluid Mech.* **45**, 269–292.
SNOEIJER, J.H., DELON, G., FERMIGIER, M. & ANDREOTTI, B. 2006 Avoided critical behavior in dynamically forced wetting. *Phys. Rev. Lett.* **96** (17), 174504.
SPELT, P.D.M. 2006 Shear flow past two-dimensional droplets pinned or moving on an adhering channel wall at moderate Reynolds numbers: a numerical study. *J. Fluid Mech.* **561**, 439–463.
SPRITTLES, J.E. 2024 Gas microfilms in droplet dynamics: When do drops bounce? *Annu. Rev. Fluid Mech.* **56** (1), 91–118.
SUI, Y., DING, H. & SPELT, P.D.M. 2014 Numerical simulations of flows with moving contact lines. *Annu. Rev. Fluid Mech.* **46**, 97–119.
THIELE, U. & KNOBLOCH, E. 2003 Front and back instability of a liquid film on a slightly inclined plate. *Phys. Fluids* **15** (4), 892–907.
VARAGNOLO, S., FERRARO, D., FANTINEL, P., PIERNO, M., MISTURA, G., AMATI, G., BIFERALE, L. & SBRAGAGLIA, M. 2013 Stick-slip sliding of water drops on chemically heterogeneous surfaces. *Phys. Rev. Lett.* **111** (6), 066101.
VOINOV, O.V. 1976 Hydrodynamics of wetting. *Fluid Dyn.* **11**, 714–721.
WANG, S., CHANG, S., ZHAO, H. & YANG, C. 2022 Dynamic behaviors of water droplet moving on surfaces with different wettability driven by airflow. *Intl J. Multiphase Flow* **154**, 104127.
WANG, N., LI, S., SHI, L., YUAN, X. & LIU, H. 2023 Viscoelastic effects on the deformation and breakup of a droplet on a solid wall in Couette flow. *J. Fluid Mech.* **963**, A18.

https://doi.org/10.1017/jfm.2026.11746 Published online by Cambridge University Press

WANG, X.L., QIN, J. & GAO, P. 2025 Axisymmetric evolution of thin films in spin coating. *J. Fluid Mech.* **1007**, A56.

XIA, Y.T., QIN, J. & GAO, P. 2020 Dynamical wetting transition on a chemically striped incline. *Phys. Fluids* **32** (2), 022101.

XU, Z., XIA, Y., HUANG, J. & LI, R. 2024 Droplet dynamics under shear flow on surfaces with different wettability. *Colloids Surf. A Physicochem. Engng Asp.* **701**, 134856.

YON, S. & POZRIKIDIS, C. 1999 Deformation of a liquid drop adhering to a plane wall: significance of the drop viscosity and the effect of an insoluble surfactant. *Phys. Fluids* **11** (6), 1297–1308.

https://doi.org/10.1017/jfm.2026.11746 Published online by Cambridge University Press